ELSEVIER

Journal of Structural Geology 29 (2007) 697–711

JOURNAL OF STRUCTURAL GEOLOGY

www.elsevier.com/locate/jsg

Mass transfer and pressure solution in deformed shale of accretionary complex: Examples from the Shimanto Belt, southwestern Japan

Kuniyo Kawabata [a,*], Hidemi Tanaka [a], Gaku Kimura [a,b]

[a] *Department of Earth and Planetary Science, The University of Tokyo, 7-3-1 Hongo, Bunkyo-ku, Tokyo 1130033, Japan*
[b] *Institute For Research on Earth Evolution, Japan Agency for Marine-Earth Science and Technology Center, 3173-25 Showa-machi, Kanazawa-ku, Yokohama-city, Kanagawa 2360001, Japan*

Received 1 January 2006; received in revised form 24 November 2006; accepted 27 November 2006
Available online 25 January 2007

Abstract

This study investigates volume changes in the accretionary complex in southeastern Shikoku, Japan using mesoscopic and microscopic observations and chemical analyses of shale. Three types of deformation in shale were recognized: 1. coherent type (compacted), 2. type I mélange (less deformed), and 3. type II mélange (sheared). Pressure solution seams (PSS) are common and reflect large volume reductions for coherent type (13–50%) and type II mélange (17–54%). Positive correlations exist between PSS density and concentration of the immobile chemical component (TiO_2) and between PSS density and paleotemperature for type II mélange and coherent type. Under constant temperature conditions, the PSS density is higher for type II mélange than for coherent type, indicating more efficient generation of PSS for type II mélange. Based on the analysis of rheological equations, we conclude that generation of PSS may be controlled by differences in differential stress and/or the duration of deformation. The positive correlation between PSS density and TiO_2 concentration indicates that volume change in accretionary complexes can be described by a simple equation using PSS density.

Keywords: Pressure solution; Isocon method; Immobile element; Volume change; Shale; Shimanto accretionary complex

1. Introduction

During accretion in subduction zones, the intense deformation that leads to the formation of structures such as imbricated folds, thrust zones and underplated mélanges is associated with large volume changes. From a microscopical point of view, such volume changes in sedimentary rocks in accretionary complexes arise from four distinct processes: (1) consolidation and cementation attributable to pore volume reduction that occurs during early accretion (e.g. Bray and Karig, 1985; Minshull and White, 1989; Moore, 1992); (2) mechanical wear from intergranular friction during cataclastic breakage of grains (Archard, 1953; Cowan, 1985; Wang and Scholz, 1994; Wong et al., 1997); (3) pressure solution deformation promoted by dissolution-precipitation mechanisms (Bjorlykke et al., 1989; Tada and Siever, 1989), which operates at the middle regime (~2 km) to the deep regime (10–15 km) in the subduction zone (Rutter, 1983; Moore, 1992); and (4) dilation formed through crack-opening. While processes (1–3) lead to volume reduction, process (4) results in volume increase, as the crack spaces become filled with precipitated secondary minerals (Brace et al., 1966; Scholz et al., 1993).

Volume changes in accretionary complexes have been estimated through observation of porosity (e.g. Bray and Karig, 1985) and finite-strain analyses in both modern accretionary prisms (e.g. Morgan and Karig, 1995) and ancient on-land prisms (Byrne and Fisher, 1987; Bolhar and Ring, 2001). Mass transfer in accretionary prisms has also been calculated through microstructural observations of fiber overgrowths from grain boundaries and deformation of paleofossils by pressure solution (Ring and Brandon, 1999). As these methods require deformation markers, calculating volume change in samples containing few markers is difficult.

* Corresponding author. Tel./fax: +81 3 5841 4599.
E-mail address: kuniyo@eps.s.u-tokyo.ac.jp (K. Kawabata).

0191-8141/$ - see front matter © 2006 Elsevier Ltd. All rights reserved.
doi:10.1016/j.jsg.2006.11.009

Another method to measure volume change is the chemical *isocon method*. Gresens (1967) first proposed equations for volume gain and loss based on the chemical composition and specific density of altered and unaltered rocks. Grant (1986) improved and simplified the method, and since then the isocon method has been widely applied to study mass and volume changes in alteration zones (Olsen and Grant, 1991; Petersson and Eliasson, 1997; Widmer and Thompson, 2001; Maghraoui et al., 2002), mineral deposits (Condie et al., 1995) and fault zones (O'Hara, 1988; Goddard and Evans, 1995; Evans and Chester, 1995; Streit and Cox, 1998; Tanaka et al., 2001; Matsuda et al., 2004; Tanaka et al., in press). However, the method has been not applied so far in altered or deformed sedimentary rocks in accretionary complexes.

Pressure solution deformation has been widely recognized in the Shimanto accretionary complexes (Ujiie, 1997; Ikesawa et al., 2005). Diffusive mass transfer associated with pressure solution may contribute to large volume changes of sedimentary rocks in accretionary prisms. A possible method to estimate such volume changes is based on the analyses of grain-shape variations and strain fringes generated by pressure solution (Ring and Brandon, 1999), but these structures are barely observable in our samples. In this study, we show that volume changes in shales from the Shimanto accretionary complex can be investigated by using the chemical isocon method. By referring to the constitutive equation of pressure solution, we discuss the controlling factors for volume changes in sedimentary rocks of accretionary complexes.

2. Geologic setting

The Shimanto Belt is an ancient accretionary complex that is located on the Pacific side of southwest Japan, subparallel to the modern Nankai Trough and the Ryukyu Trench (Fig. 1). The Shimanto Belt includes coherent, mélange, and slope-basin deposits that trend generally ENE-WSW and dip steeply to the north, with younger ages to the south (Taira et al., 1988). The coherent units consist of trench turbidite and the mélange units consist of a mixture of trench turbidite, hemi-pelagic and pelagic sediments, and basalts. The belt is divided into two sub-belts by the Aki Tectonic Line (ATL): the northern sub-belt, of Cretaceous age; and the southern sub-belt, of Tertiary age (Fig. 1a).

Numerous structural and biostratigraphic studies have been carried out in eastern Shikoku. Stratigraphic limits have been described in these studies, largely based on fossil ages. We combined geological maps of Taira et al. (1980), Hibberd et al. (1992), Ditullio and Byrne (1990), and Ishida (1998) for the stratigraphic divisions of eastern Shikoku used in the present study (Fig. 1b,c). Coastal areas from the lowest unit of the northern sub-belt (Mugi mélange) to the lowest unit of the southern sub-belt (Misaki sequence) are examined in this study (Fig. 1b–d). The Mugi mélange is a tectonic mélange of a shale matrix showing a duplex structure that includes blocks of sandstone, tuff, minor amounts of chert and basalts (Fig. 1d; Ikesawa et al., 2005; Kitamura et al., 2005). Among the units of the southern sub-belt, Ebugaike, Naharigawa, Shiina, Gyoto, Tsuro and Misaki formations comprise turbidite and show a coherent structure that includes sand and shale layers (Taira et al., 1980; Hibberd et al., 1992; Ishida, 1998). Sakamoto and Hioki units are mélanges, but their origin remains controversial (Taira et al., 1980; Ditullio and Byrne, 1990; Hibberd et al., 1992). Ditullio and Byrne (1990) argued that mélanges are tectonic in origin, but Sakai (1987) and Osozawa (2005) proposed that they are of sedimentary or diapiric origin. Fundamentally, the matrix of mélange units that have originated from both sedimentary and tectonic processes is comprised of shale.

Geothermometry by vitrinite reflectance (Mori and Taguchi, 1988; Underwood et al., 1992, 1993; Ohmori et al., 1997; Ikesawa et al., 2005) and fluid inclusion analysis (Matsumura et al., 2003) has revealed the following thermal pattern: in both Tertiary and Cretaceous sections, the indices of vitrinite reflectance increased southwards (oceanward); but thermal gaps, corresponding to large tectonic lines, exist between sequences. Paleotemperatures, based on the mean value of vitrinite reflectance, are in the range 140–315 °C in the Tertiary section (Mori and Taguchi, 1988; Underwood et al., 1992). In the Cretaceous section, the paleotemperature of the Mugi mélange formation is approximately 200 °C (Ikesawa et al., 2005). Temperature estimated from the vitrinite reflectance is consistent with those determined from fluid inclusion analysis (Matsumura et al., 2003).

3. Mesoscopic and microscopic shale structures

For this study, samples derived from each unit were classified into coherent type and mélange according to their mesoscopic structures. Cowan (1985) defined two mélange types based on mesoscopic fabrics and lithologic composition; type I mélange includes sequences of originally interbedded sandstone and mudstone; and type II mélange includes deformed, thin layers of green tuff, radiolarian ribbon chert, and minor sandstone originally inter-bedded with shale. The Mugi mélange is therefore classified as type II; Hioki and Sakamoto mélanges are regarded as type I (Fig. 1b–d).

Coherent type consists of alternating layers of sandstone and shale (Fig. 2a). Mesoscopic slump folds and sand dikes are visible (Fig. 2d–e). Microstructural observations indicate that coherent type shale comprises quartz and feldspar grains and clay minerals. Widely developed pressure solution seams (PSS) are visible along with strain fringes in strain shadows (Fig. 2h and k), indicating that pressure solution operated during deformation. The blocks in type I mélanges are composed solely of sandstone, and the shale matrix display incipient cleavage (Fig. 2b). This shale comprises angular quartz, feldspar grains, small amount (<3%) of opaque minerals, and sparsely distributed clay minerals. Minor amounts of PSS are visible along grain contacts (Fig. 2i and l). Type II mélanges are highly sheared in most sampling locations and show asymmetric deformation of the blocks of basalt, chert, and sandstone (Fig. 2c). The shale matrix in type II mélanges is cleaved by shears and PSS and shows S-C structures, in

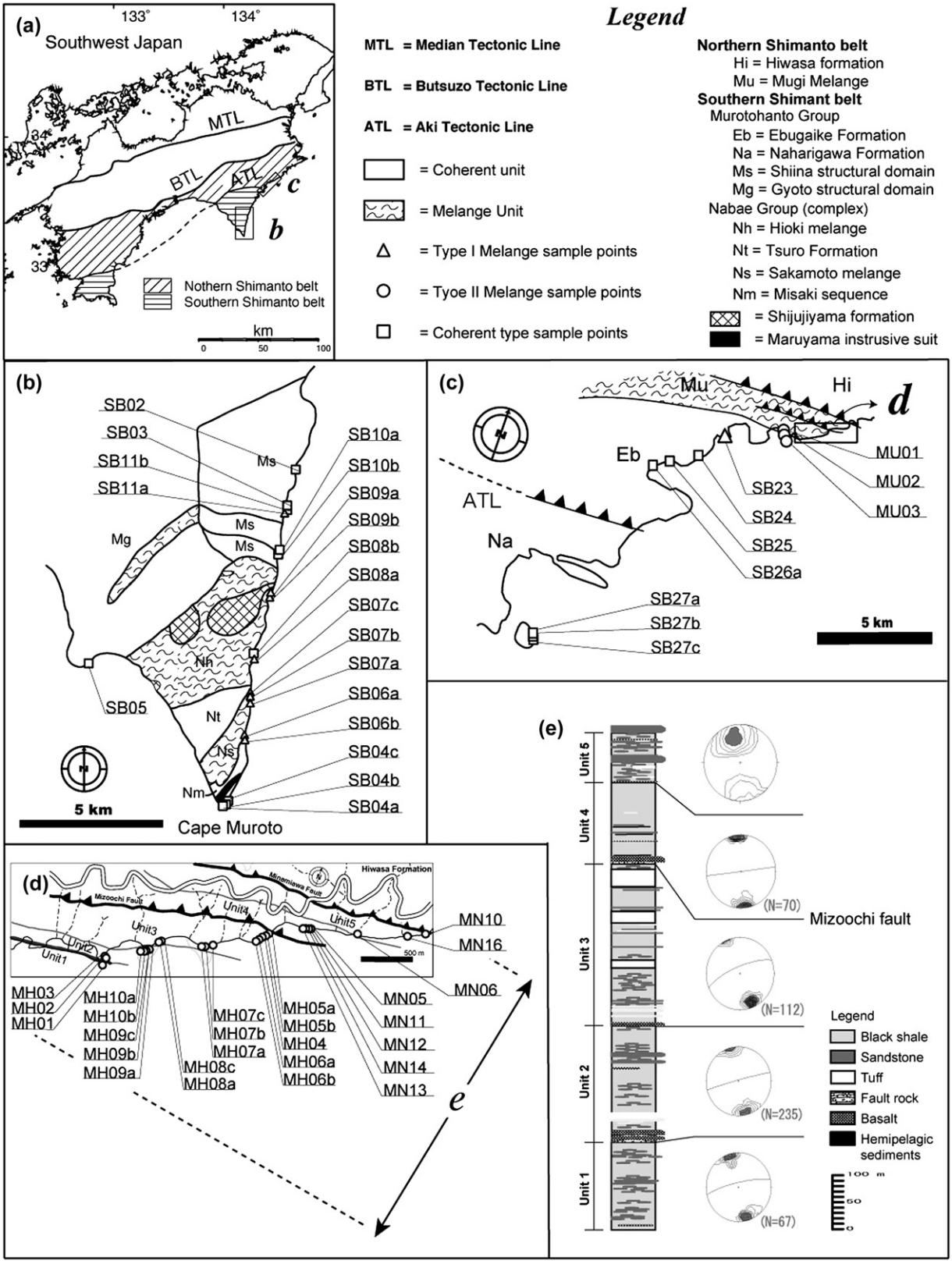

Fig. 1. Geological maps of the Shimanto Belt, southeast Shikoku, Japan: (a) basic geology of the Shimanto Belt in Shikoku Island and locations of close-ups b and c; (b) Cape Muroto and sampling locations; (c) map around the boundary fault between Shimanto northern and southern belts (ATL) and sampling locations; (d) Mugi district, Tokushima prefecture (modified from Ikesawa et al., 2005) and sampling locations; and (e) structural columnar section of the Mugi mélange and stereographic plots for foliation orientation.

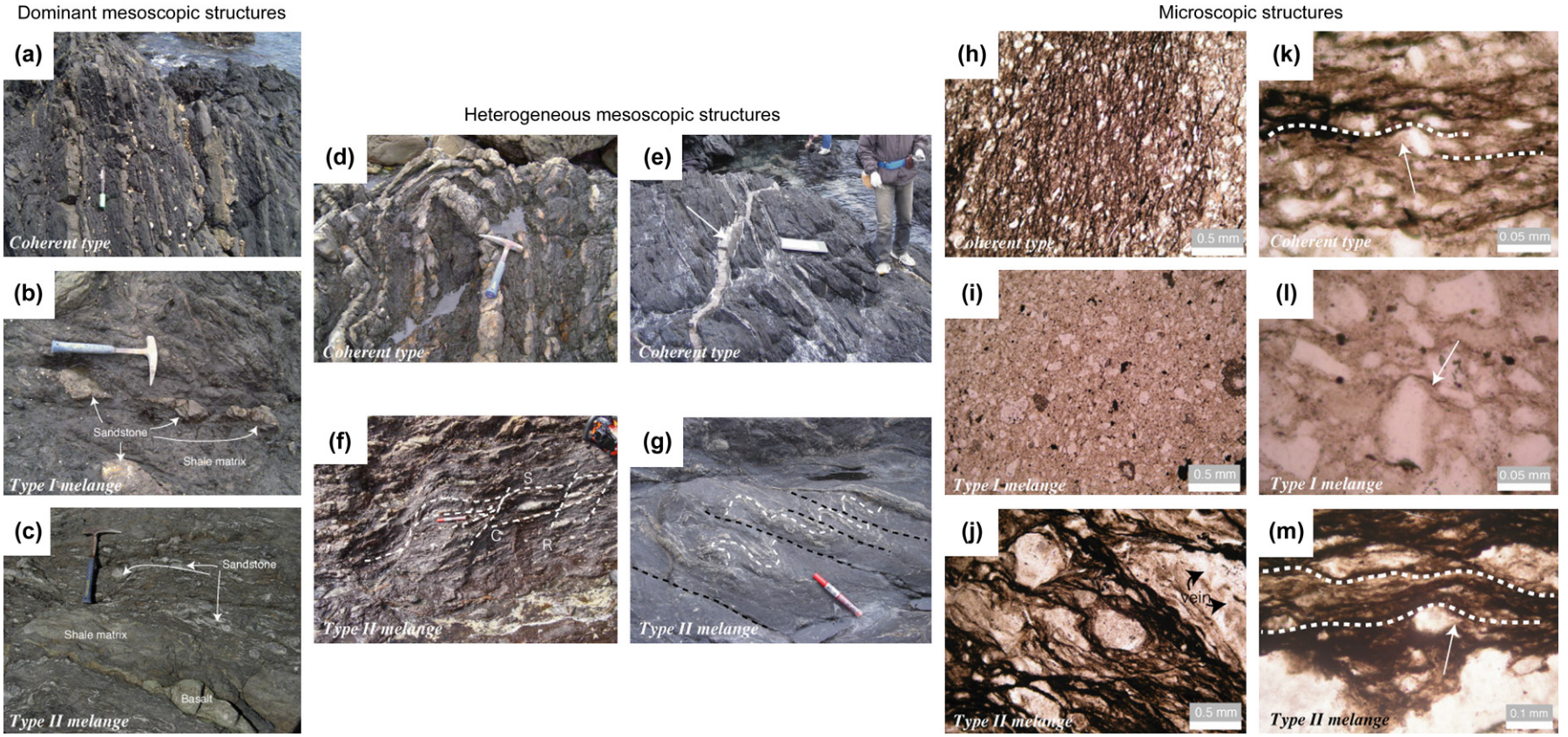

Fig. 2. Mesoscopic and microscopic structures observed in the Shimanto accretionary complex. (a) Coherent type consists of alternation of sandstone and shale. Cleavages develop in shale. (b) Type I mélange showing mélange fabric with sand block-in-shale matrix features. (c) Type II mélange showing block-in-matrix structure. Sandstone and basalt blocks are embedded in the shale matrix. (d) Meso-scale folds in coherent type. (e) Injection of a sand dike in coherent type. Arrow shows sand dike. (f) Intensely developed S-C structures in shale of type II mélange. Dashed lines show local traces of S, C, and R (Riedel) surfaces. S surfaces are apparently almost parallel to C surfaces. (g) Folds and faults structure in shale of type II mélange. White dashed lines show local traces of folds; black dashed lines indicate faults. (h) Microscopic structure of shale in a coherent type. Pressure solution seams (dark seams) are visible. (i) Microscopic structure of matrix shale in type I mélange. Deformation is weak. (j) Microscopic structure of matrix shale in type II mélange. Numerous PSS are visible. Black arrows show micro-veins in boudinaged sandstone. (k) Enlarged microphotograph of (h), grains' long axes are roughly parallel to dark seams. Minor fibrous overgrowth is visible. Dashed lines show local traces of dark seams and arrows show overgrowth. (l) Enlarged microphotograph of (i): a few dark seams are visible. The arrow shows tiny fiber overgrowth from quartz grain. (m) Enlarged microphotograph of (j), thick dark seams are visible and grains' long axes are arranged parallel to dark seams. Fibrous overgrowths are visible. Dashed lines show local traces of dark seams and the arrow indicates fibrous overgrowth.

which S surfaces are mostly sub-parallel to C surfaces (Fig. 2f). Mesoscopic folds and faults are visible in the matrix shale, in which faults separate numerous layers of sandstone (Fig. 2g). Foliation is generally ENE-WSW and dips steeply northward (Fig. 1e). The shale is composed of quartz, feldspars, and clay minerals. Micro-boudinaged sandstone fragments also occur (Fig. 2f). They are highly sheared and contain quartz-filled cracks (Fig. 2j), widely developed PSS parallel to the foliation and strain shadows (Fig. 2m).

Microscopic observations show that the three types are almost identical litologically, and that foliations are defined by preferred alignments of minerals and/or shear surfaces such as S, C, and R surfaces. PSS is more abundant in samples from type II mélange and coherent type than those from type I mélanges.

In total, 55 samples were collected from shales in each unit showing homogeneous structures. Samples were not taken from outcrops showing heterogeneous structures, as shown in Fig. 2d–g.

4. Pressure solution seams in shale

4.1. Chemical characteristics of PSS

The pressure solution seams (PSS) are residues that arise from dissolution of materials from grain contact surfaces and asperities (e.g. Rutter, 1983). Chemical mapping analysis using Electron Probe Micro-Analyzer (JXA-8900L; JEOL) was performed to assess the element concentration in PSS.

Goldschmidt (1954) showed that the solubility of elements in H_2O depends on the ion potential. Elements with smaller ion potential are more soluble; high field-strength elements like Ti, Zr, and Nb are only slightly soluble in H_2O. Several elements are putatively immobile, even under intense pulverization and alteration conditions in fault zones. As examples, O'Hara (1988) treated TiO_2, P_2O_5, Zr, Y, and V as immobile elements in ultramylonite shear zones; Evans and Chester (1995) described TiO_2, P_2O_5, MgO, MnO, Zr, and Y as immobile elements in brittle shear zones pervaded by fluids; Goddard and Evans (1995) inferred TiO_2, Fe_2O_3, MgO, and Zr to be immobile elements in fluid-filled shear zones; and Tanaka et al. (2001, in press) described TiO_2 and P_2O_5 as immobile elements in material obtained from a fluid-saturated active fault zone. All of those studies empirically showed that TiO_2 is an immobile element.

We performed Chemical mappings of Ti, Fe, P, and Zr, along with Si, for reference. Four samples (SB02, SB03, SB05, and MH03) were chosen to investigate various occurrences of PSS (Fig. 3a–d): MH03 (type II mélange) shows an anastomosing network of PSS (Fig. 3a); SB02 (coherent type) contains discrete, thick PSS (100 μm) (Fig. 3b); SB05 (coherent type) shows pervasive PSS (Fig. 3c); and SB03 (coherent type) contains few PSS (Fig. 3d). Chemical mapping reveal markedly higher titanium contents within PSS in SB02, SB05, and MH03 (Fig. 3e–h), although Si, Fe, and Zr concentrations do not differ from those of the host material. Phosphorus is concentrated in PSS only in SB02 (Fig. 3j). These results indicate that only Ti was an insoluble element with respect to pressure solution deformation, which concurs with all the previous studies in fault rocks.

4.2. Relationship between PSS density and paleotemperature

We define the PSS density as the ratio of PSS-occupied area over the total area in a thin section photograph; it is taken as an index of the pressure solution deformation intensity. The PSS density is calculated as follows. (1) Repaint opaque minerals white using graphic software. (2) Designate PSS as black areas in a binarized photomicrograph. (3) Count black pixels and normalize that quantity by the total photograph area.

Along with the determination of PSS density, paleotemperatures during pressure solution deformation were determined by Kitamura et al. (2005) for the Mugi mélange of the Cretaceous age and by Mori and Taguchi (1988) for the Tertiary Shimanto Belt using vitrinite reflectance. The PSS measurement distance errors arising from different sampling location between this study and that of Kitamura et al. (2005) are ±2 m in the Mugi mélange area. However, the location error might be ±50 m in other formations because of the different map scales used in this study and that of Mori and Taguchi (1988).

Sakaguchi (1996, 1999) suggested that a heating event took place during Tertiary accretion based on results of vitrinite reflectance. Ditullio and Byrne (1990) also suggested that in the southern part of the Tertiary Shimanto Belt (Gyoto and Shiina domains) pressure solution cleavages developed in periods of high temperature. Similarly, we consider here that the pressure solution deformation visible in our samples occurred during a high-temperature event of Tertiary age. For Cretaceous section, the temperature was estimated in the range 125–195 °C by fluid inclusions analysis in crack-seal veins (Matsumura et al., 2003), which is consistent with 130–200 °C range measured by using vitrinite reflectance (Kitamura et al., 2005). The PPS in shale overprint the crack-seal veins in necked boudinaged sandstone. Therefore, pressure solution would be slightly subsequent to the stage with thermal condition around 125–195 °C. Those inferences imply that vitrinite reflectance is correlated with pressure solution deformations in both the Tertiary and Cretaceous Shimanto complexes.

The PSS density in type II mélange and those of coherent type are well correlated with vitrinite reflectance (Fig. 4), indicating that PSS development is controlled fundamentally by temperature; nevertheless, the data are insufficient to infer an appropriate correlation for type I mélange. The regression line slope is steeper for type II mélange than for coherent type. We will discuss on this topic later in Section 6.1.

5. Chemical composition analysis

5.1. Bulk chemical composition of shale

Tiny fragments of sandstone, basalt, tuff, and chert and veins were removed from all samples. The remaining shale was powdered. In total, 55 powder samples were prepared to

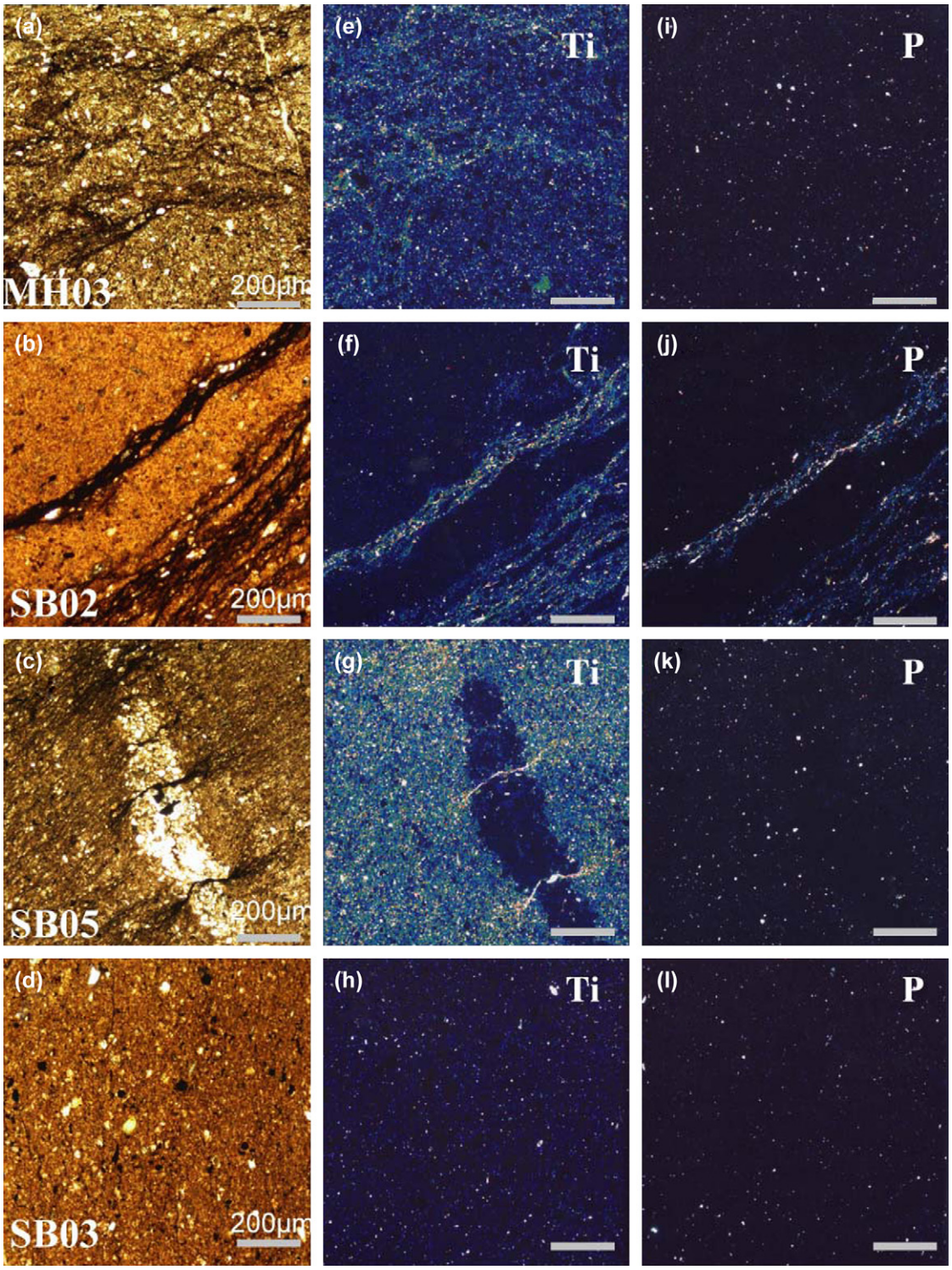

Fig. 3. Microphotographs of PSS in thin sections and chemical (Ti and P) mapping results. (a)–(d) optical microscopic photographs of PSS (dark seams). Microphotographs of (e)–(h) and from (i)–(l) respectively show chemical mapping results for titanium and phosphorus. (a) Anastomosing occurrence of PSS in sample MH03 (type II mélange). (b) Occurrence of PSS in sample SB02 (coherent type). (c) Micro-foliations form in association with the PSS in sample SB05 (coherent type). (d) No PSS is visible in sample SB03 (coherent type).

assay for major and trace element compositions through whole-rock X-ray fluorescence methods (XRF: PW1480). Major elements are measured using the fused glass bead method and are presented as weight oxide proportions. Trace elements are quantified using the powder press method. Loss on ignition (LOI) is also measured using weight changes on heating at 1000 °C for 8 h. The weight ratio of major elements and LOI are combined and normalized to 100 wt%. Grain densities of crushed samples were measured using the pycnometer method (Auto True Denser, MAT-5000).

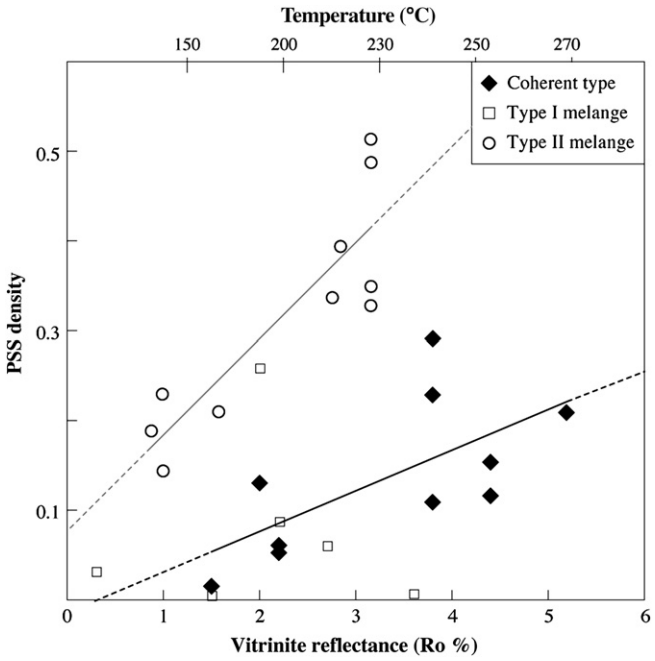

Fig. 4. Relationship between vitrinite reflectance and PSS density. The vitrinite reflectance is shown as Ro % (average of measured values). Solid squares, open squares and open circles correspond respectively to coherent type, type I mélange and type II mélange. Coherent type and type II mélange show good correlation between vitrinite reflectance and the PSS density.

Table 1
Average of bulk chemical compositions, assumed chemical compositions for host rock and grain densities

	Averaged compositions			Assumed compositions of host rock	
	Coherent type	Type I melange	Type II melange	Coherent type	Type II melange
Grain density (g/cm^3)	2.68	2.68	2.69	2.68	2.69
Major elements (wt%)					
SiO_2	65.27	69.42	65.91	67.55	74.17
TiO_2	0.76	0.57	0.63	0.52	0.36
Al_2O_3	16.97	14.17	15.96	14.28	10.12
Fe_2O_3	5.12	4.59	5.54	5.71	5.45
MnO	0.04	0.05	0.18	0.05	0.18
MgO	1.77	1.56	1.90	1.90	1.87
CaO	0.40	0.58	0.55	0.46	0.54
Na_2O	1.81	2.02	2.25	1.76	2.21
K_2O	3.72	2.77	3.25	3.54	1.38
P_2O_5	0.12	0.09	0.10	0.13	0.05
LOI	4.01	4.19	3.73	4.09	3.67
Trace elements (ppm)					
Ba	467.8	349.0	262.9	467.8	262.9
Ni	35.3	26.6	35.9	35.3	35.9
Cu	42.8	29.5	73.0	42.8	73.0
Zn	108.0	90.0	113.1	108.0	113.1
Pb	20.3	21.2	24.2	20.3	24.2
Th	14.8	12.5	15.2	11.8	4.5
Rb	150.0	116.8	136.9	150.0	136.9
Sr	97.9	100.8	93.7	97.9	93.7
Y	23.4	21.1	23.7	23.4	10.6
Zr	212.5	227.7	203.9	212.5	203.9
Nb	11.6	9.3	10.7	7.8	3.4

Data tables of chemical composition and grain density are presented in the Appendix. Table 1 shows average chemical compositions for the shale of each type. Average coherent type components resemble those of type II mélange, except for MnO. Type I mélange contains higher SiO_2 than other types. The compositional variations that we analyze hereafter (Section 5.2 and Fig. 6) are relatively small and show a unimodal distribution with low standard deviations (Fig. 5a–k). The grain density varies in the range 2.65–2.76 g/cm^3, average 2.69 g/cm^3 (Fig. 5l).

5.2. Estimation of volume changes using the isocon method

TiO_2 content is well correlated with PSS density in type II mélange and coherent type (Fig. 6a). Data for TiO_2 in type I mélange are not shown because of its poor correlation with PSS density, which might be attributable to the small number of analyses. The chemical composition results indicate that TiO_2 is insoluble during pressure solution deformation. As a result, the isocon method using TiO_2 as an immobile reference frame was applied to deformed shale of the Shimanto accretionary complex.

Other immobile elements reported in previous studies are examined in this study through comparison to TiO_2 (Fig. 7a–h). Elements correlating well with TiO_2 can be regarded as immobile during pressure solution deformation. Only Nb and Al_2O_3 show a strong correlation with TiO_2. Although Nb was already reported as an immobile element during deformation, this study shows a similar behavior for Al_2O_3. On the other hand, all other analyzed elements, even P and Th, are only weakly or not at all correlated with TiO_2 and cannot therefore be considered as immobile.

We applied the isocon method using TiO_2, Al_2O_3 and Nb as an immobile reference frame, and estimated the volume loss/gain of the shale in coherent type and type II mélange. The volume changes for type I mélange cannot be calculated because the PSS density is not well correlated with TiO_2.

Composition of the original undeformed rock (host rock) is not directly measurable because all samples show some deformation. Therefore, we estimated the chemical composition of the host rock using a correlation diagram which includes chemical composition and PSS density (Fig. 6). For constituents showing good correlation with PSS density (correlation coefficient >0.8), the host rock composition is discernible by extrapolating the correlation lines to 0% PSS density. Such constituents are, for coherent type, SiO_2, Al_2O_3, P_2O_5, Th, and Nb; and for type II mélange, SiO_2, Al_2O_3, K_2O, P_2O_5, Y and Nb. For other elements, variations which are not correlated with PSS density and therefore are not related to deformation may reflect the natural variability in host rock. As a result, we determined the content of such constituents by simply averaging over our analyzed samples. By combining extrapolated and averaged weight percents and

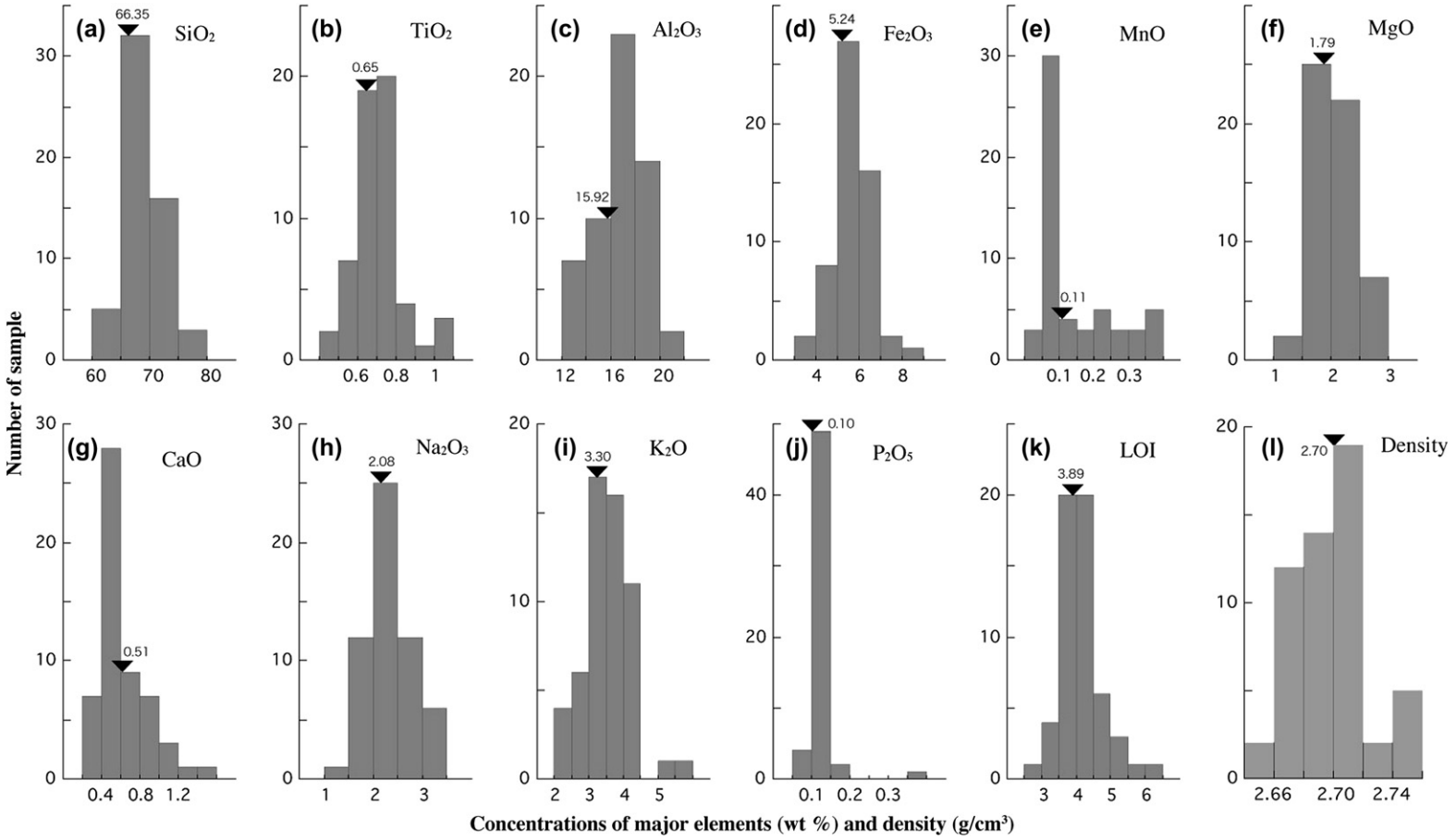

Fig. 5. Histograms showing the distribution of major chemical elements and grain densities of the 55 analyzed shale samples. Solid triangles indicate average values. (a)–(k) The distribution of major elements shows a nearly unimodal shape, indicating homogeneous chemical composition of the shale. (l) Distribution of grain densities for all samples.

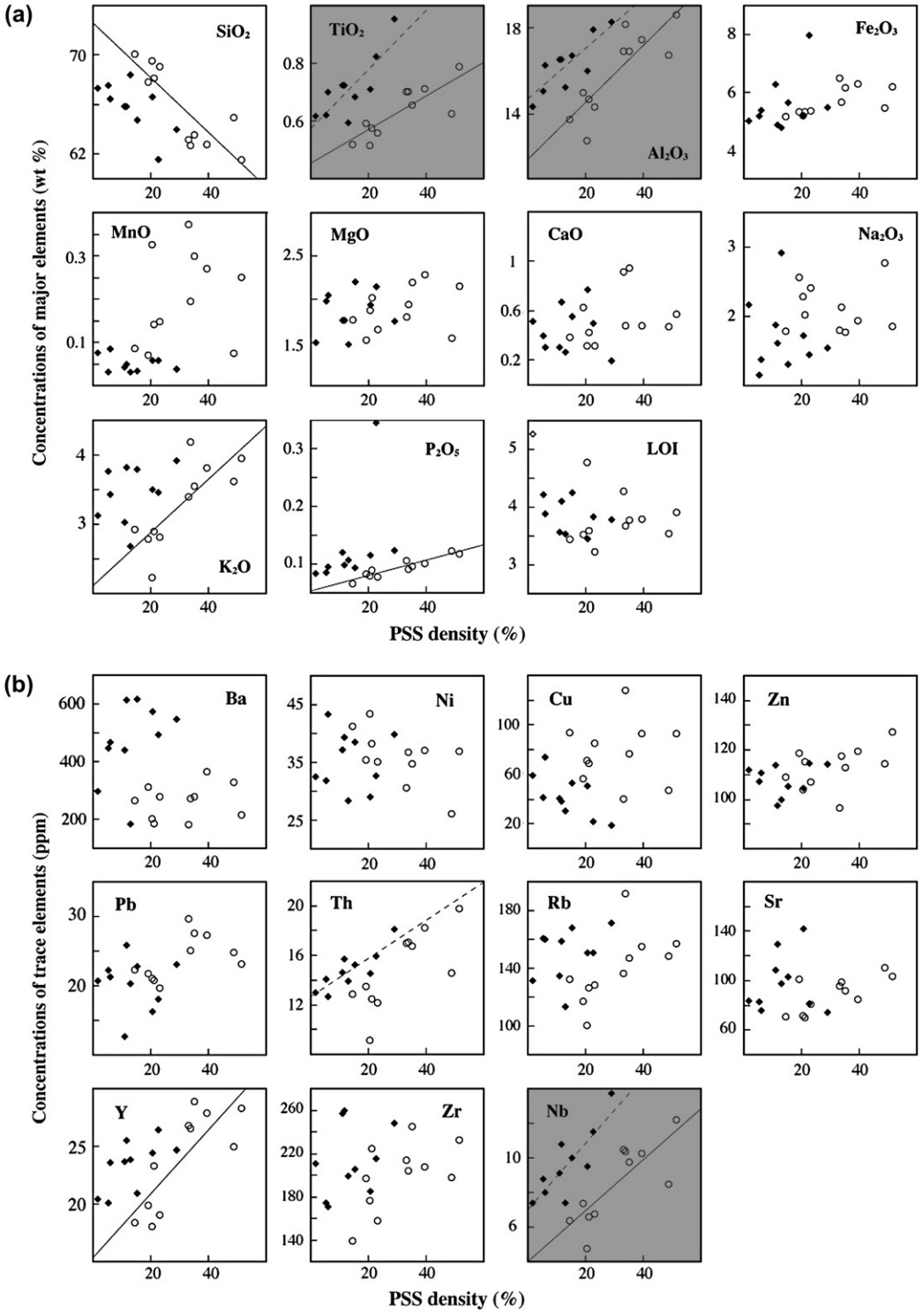

Fig. 6. Relationship between PSS density and concentrations of (a) major and (b) trace elements. The solid diamond shows coherent type and the open circle shows type II mélange. Broken (coherent type) and black lines (type II mélange) are assigned to data that show a good correlation ($R > 0.8$). The diagrams with a gray background are immobile elements used in this paper based on the results shown in Fig. 7.

normalizing them to 100 wt%, chemical compositions of host rocks were estimated for coherent type and type II mélange. Average density values are similar among all types (Fig. 5l). Consequently, we use an average grain density of 2.7 g/cm^3 as the grain density of the host rock for both coherent type and type II mélange.

Estimating host rock composition and grain density enables us to use Grant's (1986) method to determine volume changes of deformed shale. When the concentration of some elements change during deformation of a given mass of host rock, the relationship between concentration of elements in the deformed rock and host rock is described as

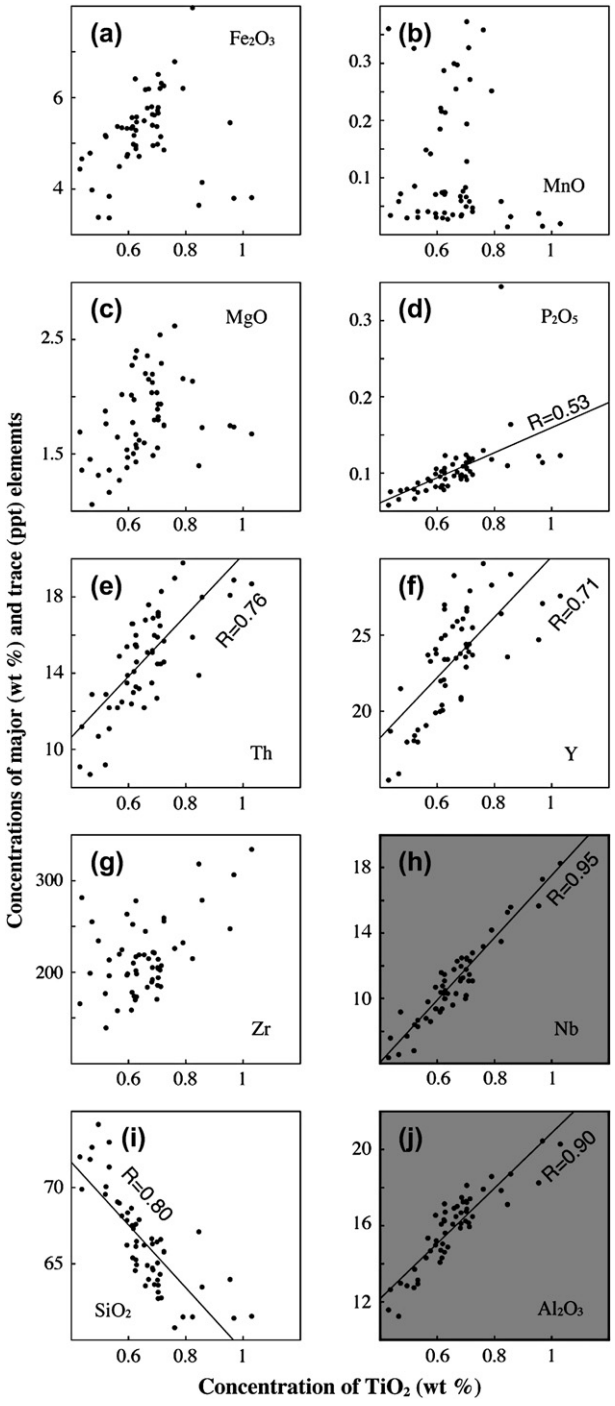

Fig. 7. The relationship between concentration of TiO_2 and the immobile chemical components reported in previous studies ((a)–(h)) and (i) SiO_2 and (j) Al_2O_3. Black lines are drawn when correlations are recognized. Al_2O_3 and Nb are well correlated with TiO_2 (gray background diagrams). Consequently, TiO_2, Al_2O_3, and Nb are regarded as immobile elements in this study.

$$C_i^d = \frac{M_h}{M_d}\left(C_i^h + \Delta C_i\right) \tag{1}$$

where C_i is the concentration of component i, M is the bulk mass, ΔC_i is change of weight percent of component i, and superscripts for h and d respectively denote host rock and deformed rock. Using Eq. (1), the normalized mass change, $\Delta M = (M_d/M_h) - 1$ is expressible using the following equation:

$$\Delta M = \left(\frac{C_i^h + \Delta C_i}{C_i^d}\right) - 1. \tag{2}$$

Considering component (i) as immobile, $\Delta C_i = 0$, yields

$$\Delta M = \left(\frac{C_i^h}{C_i^d}\right) - 1. \tag{3}$$

The normalized volume change, $\Delta V = (V_d/V_h) - 1$, is obtainable using Eq. (3) and the grain density of samples as

$$\Delta V = \left(\frac{C_i^h}{C_i^d}\frac{\rho^h}{\rho^d}\right) - 1, \tag{4}$$

where ρ is the grain density.

Results of estimated volume changes are also shown in the Appendix and are summarized in Fig. 8. Volume changes are −13 to −50% (average −30%) in coherent type and −17 to −54% (average −43%) in type II mélanges (Fig. 8).

5.3. Relationship between volume change and deformation intensity

Lithologic differences between coherent type and type II mélange lead to large differences in TiO_2 content (Fig. 6a). Nevertheless, estimating the bulk rock composition of TiO_2 as explained above allows us to normalize the TiO_2 variations in both coherent and type II mélange (Fig. 9). As a result, the

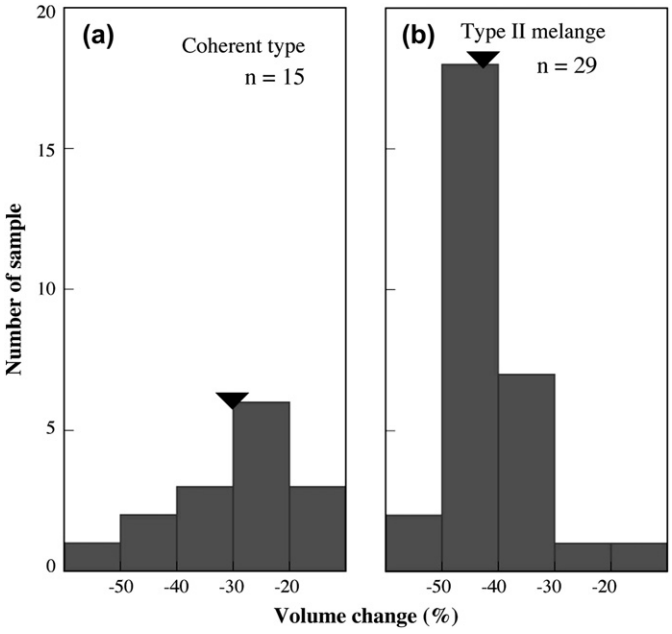

Fig. 8. Histograms of volume change. Solid triangles show the average percentage and n is the number of samples that were averaged. (a) The volume change in coherent type is −13 to −50% (average −30%). (b) The volume change in type II mélange is −17 to −54% (average −43%).

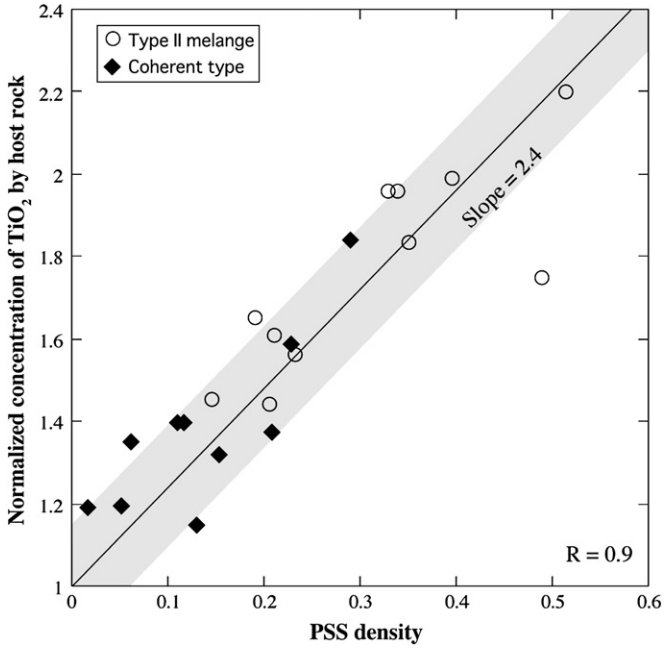

Fig. 9. Relationship between PSS density and normalized concentrations of TiO_2 by host rock. Solid diamonds show a coherent type and open circles show type II mélange. The inclination of the slope is 2.4 and R is 0.9. Gray colored area is the range of standard deviation of regression line (±0.14). The volume loss is estimated from the TiO_2 concentration (see Section 6.1.3 for a detailed explanation).

relation between deformation (measured as PSS density) and normalized TiO_2 appear to be governed by a single law, which is independent of the type of rock considered. Therefore, using the empirical law derived in the Section 6.1.3, volume changes can easily be estimated from the analysis of PSS density.

6. Discussion

6.1. Development of pressure solution seams in deforming shales

6.1.1. Controlling factors for PSS development

The constitutive equation of pressure solution is

$$\frac{de}{dt} = A \cdot \frac{\sigma \cdot w \cdot D \cdot S \cdot V}{R \cdot T \cdot d^3}, \tag{5}$$

where e is the strain, A is a numerical coefficient, σ is the differential stress, w is the width of grain boundary film, D is a diffusion coefficient of dissolved solid in the film, S is the solid's solubility in the film, R is the gas constant, T is the temperature, V is the solid's molar volume, and d is the grain diameter (Coble, 1963; Rutter, 1976; Raj, 1982; Spiers et al., 1990). The parameters in this equation suggest a complex influence of temperature on the strain rate: temperature is used in the denominator but is also strongly related to both diffusion coefficient D and solubility S.

This study shows positive correlations between the PSS density and paleotemperature in type II mélange and coherent type (Fig. 4), indicating that increased temperature tends to promote pressure solution. However, the correlation line slope for PSS density in type II mélange is greater than that for coherent type. To explain these differences, we examined the influence of parameters other than temperature. If the temperature T is given, parameters D and S will be constant and similar between coherent type and type II mélange, because Spiers et al. (1990) shows

$$D \cdot S = D_0 \cdot S_0 \cdot \exp(-\Delta H/RT), \tag{6}$$

where D_0 and S_0 are reference values of D and S in the limit $1/T \rightarrow 0$ and ΔH is activation energy. Activation energy has been estimated to be 70 ~ 80 kJ/molK (Gratier and Jenatton, 1984; Schutjens, 1991; Niemeijer et al., 2002), and then ΔH can be approximated as a constant. Thus, the Eq. (6) indicates that $D \cdot S$ might be constant under a certain temperature. PSS show a relatively constant thickness within our samples. We assume that PSS density is proportional to the strain ($\gamma_{PSS} = \alpha \cdot e$), where γ_{PSS} is the PSS density and α is a constant. Grain size determination within PSS is difficult in natural shale because of very large size variations within a single sample. For this study, grain sizes of type II mélange and coherent type are assumed to be similar. Consequently, the equation can be simplified as

$$\gamma_{PSS} = A' \cdot \sigma \cdot t. \tag{7}$$

Therein, $A' = A \cdot \alpha \cdot D \cdot S \cdot w \cdot V/(R \cdot T \cdot d^3)$ is a constant. The differences of the linear coefficients of the PSS density/temperature curves between type II mélange and coherent type in Fig. 4 may be related to differences in stress and duration of pressure solution deformation. Such variations may be related to the very different processes of formation and history of the two units. Coherent units are formed by offscraping processes at shallow levels of accretionary prisms (Taira et al., 1988; Ditullio and Byrne, 1990) in the Tertiary, whereas tectonic mélange was eventually deeply underplated in the Cretaceous (Matsumura et al., 2003; Ikesawa et al., 2005). During offscraping processes, sedimentary rocks are compressed by the subducting oceanic plate with the formation of E-W trending folds and thrust structures. In contrast, tectonic mélanges underwent larger shear stress near the plate interface of the subduction zone (Kitamura et al., 2005). In addition, it is possible that the duration of the deformation of the tectonic mélange (type II mélange) is significantly longer, as the coherent type rocks were quickly off-scraped under the accretionary prism, while mélange rocks were deformed much further within the subduction zone before being accreted to the hanging plate by underplating (Kitamura et al., 2005).

6.1.2. Volume loss associated with pressure solution deformation

Volume changes calculated using the isocon method range from −13 to −50% in coherent type and from −17 to −54% in type II mélanges (Fig. 8). It may be surprising that the largest volume loss in the coherent type is comparable to that in shale of type II. Nevertheless, coherent type rocks are strongly heterogeneous, as they consist of rheologically contrasting

layers of sandstone and shale. Therefore, it is likely that the deformation within the coherent type rock is also strongly heterogeneous at all scales, and that some samples of coherent type may have been subjected to deformation of similar intensity as mélange samples.

6.1.3. Constitutive relationship between PSS density and volume change

The linear relationship between PSS density (γ_{PSS}) and normalized TiO_2 ($C^d_{TiO_2}/C^h_{TiO_2}$) (Fig. 9) suggests that

$$C^d_{TiO_2}/C^h_{TiO_2} = 2.4 \cdot \gamma_{PSS} + 1. \quad (8)$$

In the Eq. (8), standard deviation of regression line is 0.14, which is shown in Fig. 9 as a gray colored range. Volume changes are $(V^d - V^h)/V^h = (C^h_{TiO_2}/C^d_{TiO_2})(\rho^h/\rho^d) - 1$. In the rocks investigated, the variation between grain density of host rock and deformed rock are relatively small, in agreement with Goddard and Evans (1995) who reported changes of grain density between host rock and deformed rock smaller than 5%. As a result, if we assume that $\rho^h/\rho^d = 1$, the volume change is expressed as

$$\Delta V = -\frac{2.4 \cdot \gamma_{PSS}}{2.4 \cdot \gamma_{PSS} + 1}. \quad (9)$$

Although further validation using a broader range of samples from different settings is probably necessary, we propose that this equation enables the estimation of volume change from the PSS density in accretionary complexes.

7. Conclusions

We demonstrated that Ti, Al, and Nb behave as an immobile element during pressure solution deformation of shale of accretionary complex. Results of isocon analyses for various shale samples from the Shimanto accretionary complex showed that the normalized TiO_2 content is proportional to PSS density, indicating that volume reduction as great as 50% occurs through pressure solution deformation. We propose a simple relationship enabling to assess volume changes from the PSS density. Comparison with the vitrinite reflectance demonstrates that pressure solution deformation is promoted by temperature in the range 130–270 °C.

Acknowledgments

We thank Yujin Kitamura and Celia Tiemi Onishi, who discussed the mesostructure and microstructure in the Mugi area of Tokushima prefecture. Constructive comments by an anonymous reviewer and Kohtaro Ujiie and by the editor Joao Hippertt are greatly appreciated. This research was funded mostly by the 21st century COE program in Department of Earth and Planetary Science, The University of Tokyo. Thanks should be extended to Institute For Research on Earth Evolution, Japan Agency for Marine-Earth Science and Technology Center (IFREE, JAMSTEC), which partly funded our research.

A. Appendix

Grain density, PSS density, volume change and bulk chemical compositions of samples

Type	Coherent type													
Sample No.	SB24	SB25	SB26a	SB27a	SB27b	SB27c	SB02	SB03	SB11b	SB10a	SB10b	SB08b	SB04a	SB04b
Grain density (g/cm^3)	2.68	2.70	2.70	2.67	2.67	2.68	–	2.72	2.69	2.73	2.75	2.71	2.74	2.71
PSS density (%)	13.1	–	6.1	–	–	–	–	5.2	–	11.7	15.3	1.6	11.0	29.1
Volume change (%)	−13.9	−21.0	−26.1	−50.4	−39.5	−47.1	–	−16.2	−39.9	−27.9	−23.0	−15.9	−27.5	−45.7
Major elements (wt%)														
SiO_2	68.40	66.25	66.46	61.57	67.12	61.45	84.61	67.52	63.49	65.82	64.74	67.34	65.80	63.98
TiO_2	0.59	0.65	0.70	1.03	0.84	0.97	0.149	0.62	0.86	0.72	0.68	0.62	0.72	0.95
$A1_2O_3$	15.23	16.09	16.27	20.31	17.14	20.48	3.08	15.06	18.73	16.50	16.71	14.32	16.51	18.25
Fe_2O_3	4.77	5.50	5.37	3.82	3.66	3.81	1.334	5.18	4.16	4.86	5.63	4.99	6.27	5.46
MnO	0.03	0.04	0.08	0.02	0.01	0.02	0.051	0.03	0.03	0.05	0.03	0.07	0.04	0.04
MgO	1.47	1.60	2.04	1.68	1.40	1.74	1.914	1.98	1.74	1.75	2.20	1.50	1.76	1.75
CaO	0.26	0.26	0.30	0.31	0.35	0.27	2.227	0.40	0.47	0.67	0.55	0.52	0.31	0.19
Na_2O	2.92	2.27	1.38	1.86	2.11	1.55	0.230	1.15	1.77	1.61	1.30	2.16	1.88	1.55
K_2O	2.68	3.09	3.43	5.25	4.13	5.19	0.519	3.76	4.17	3.82	3.80	3.13	3.03	3.92
P_2O_5	0.11	0.11	0.10	0.12	0.11	0.11	0.193	0.08	0.16	0.10	0.09	0.08	0.12	0.12
LOI	3.53	4.13	3.88	4.03	3.11	4.41	5.700	4.22	4.43	4.10	4.25	5.27	3.56	3.79
Trace elements (ppm)														
Ba	183	261	468	576	434	434	–	447	671	612	616	296	442	548
Ni	28.4	31.7	43.3	27.0	25.9	30.2	–	31.9	24.3	39.3	38.5	32.5	37.2	39.8
Cu	30.6	35.8	73.9	33.4	18.3	34.0	–	41.5	33.9	38.0	52.6	58.9	40.4	19.0
Zn	100	130	111	100	103	108	–	107	98	98	105	112	114	114
Pb	20.3	22.5	21.3	27.4	21.1	21.7	–	22.2	19.7	25.8	22.8	20.7	12.6	23.1
Th	13.9	12.2	12.7	18.7	13.9	18.9	–	14.1	18.0	15.7	15.2	13.0	14.6	18.1
Rb	113	123	160	197	157	212	–	160	176	159	168	131	135	171
Sr	97.5	104.2	76.0	148.1	150.4	137.6	–	83.1	128.1	129.4	103.2	83.5	108.1	74.5
Y	23.8	25.6	23.6	27.6	23.6	27.1	–	20.1	29.0	25.5	20.9	20.4	23.7	24.7

A. Appendix (*continued*)

Type	Coherent type													
Sample No.	SB24	SB25	SB26a	SB27a	SB27b	SB27c	SB02	SB03	SB11b	SB10a	SB10b	SB08b	SB04a	SB04b
Zr	199	219	171	335	319	307	–	174	279	260	206	211	257	248
Nb	9.4	9.6	10.0	18.3	15.3	17.3	–	10.8	15.6	12.8	12.0	9.4	11.1	15.7
Type	Coherent type		Type II melange											
Sample No.	SB04c	SB05	MN10	MN16	MN06	MN05	MN14	MN12	MN11−1	MN11−2	MN13	MH05a	MH05b	MH04
Grain density (g/cm^3)	2.76	2.74	2.71	2.70	2.74	2.73	2.71	2.70	2.68	–	2.71	2.68	2.68	2.67
PSS density (%)	22.8	20.8	33.8	–	39.5	35.0	–	32.9	–	–	51.4	–	48.8	23.1
Volume change (%)	−35.9	−26.3	−49.4	−49.1	−50.7	−46.2	−46.8	−49.2	−41.2	–	−55.0	−48.7	−42.6	−35.6
Major elements (wt%)														
SiO_2	61.56	66.61	62.75	63.61	62.80	63.57	63.99	63.17	65.40	60.82	61.53	63.94	64.97	69.08
TiO_2	0.82	0.71	0.70	0.70	0.71	0.66	0.67	0.70	0.61	0.76	0.79	0.70	0.63	0.56
$A1_2O_3$	17.87	15.96	18.15	17.24	17.44	16.92	17.02	16.91	16.11	17.92	18.62	17.30	16.75	14.32
Fe_2O_3	7.97	5.16	5.67	5.79	6.32	6.17	6.20	6.52	5.37	6.79	6.21	5.72	5.48	5.37
MnO	0.06	0.06	0.19	0.13	0.27	0.30	0.30	0.37	0.22	0.36	0.25	0.07	0.07	0.15
MgO	2.14	1.94	1.94	1.83	2.29	2.20	2.16	1.80	1.78	2.62	2.16	1.89	1.56	1.65
CaO	0.49	0.77	0.49	0.74	0.48	0.95	0.61	0.92	1.36	1.17	0.57	0.30	0.47	0.32
Na_2O	1.44	1.72	2.13	2.09	1.95	1.78	1.86	1.81	2.94	2.38	1.86	2.17	2.77	2.41
K_2O	3.46	3.50	4.20	3.77	3.82	3.56	3.54	3.41	2.65	3.50	3.96	3.84	3.63	2.82
P_2O_5	0.35	0.12	0.09	0.11	0.10	0.10	0.10	0.11	0.10	0.13	0.12	0.11	0.12	0.08
LOI	3.83	3.45	3.69	4.00	3.81	3.79	3.54	4.29	3.46	3.54	3.92	3.96	3.55	3.23
Trace elements (ppm)														
Ba	493	573	274	234	367	280	350	183	212	202	216	345	332	281
Ni	32.6	29.0	36.8	32.8	37.2	34.8	39.1	30.6	34.7	43.3	37.0	35.0	26.1	35.1
Cu	21.9	50.7	128.0	79.1	93.4	77.4	85.0	40.4	45.7	82.5	93.3	98.8	47.8	85.5
Zn	115	105	118	105	120	113	115	97	93	122	128	119	115	107
Pb	18.0	16.3	25.1	27.1	27.4	27.7	23.3	29.7	53.4	18.9	23.2	25.8	24.9	19.7
Th	15.9	14.5	17.1	17.2	18.3	16.8	17.6	17.0	16.6	19.0	19.8	15.9	14.6	12.2
Rb	151	151	192	155	155	147	148	136	110	141	157	166	149	128
Sr	81.1	142.1	99.0	75.6	85.3	91.9	96.0	96.2	178.1	135.4	104.2	90.0	110.5	81.0
Y	26.4	24.4	26.6	24.2	27.9	28.9	25.9	26.8	24.8	29.7	28.3	22.9	25.0	19.1
Zr	215	185	204	194	208	245	215	214	253	226	233	186	198	159
Nb	13.5	11.5	12.4	12.4	12.3	11.8	12.3	12.5	11.6	13.2	14.2	11.8	10.5	8.8
Type	Type II melange													
Sample No.	MH06a	MH06b	MH07a	MH07b	NH07c	MH08a	MH08c	MH09a	MH09b	MH09c	MH10a	MH10b	MH03	MH01
Grain density (g/cm^3)	2.66	2.68	2.71	2.69	2.69	2.67	2.67	2.67	2.67	2.66	2.67	2.69	2.69	2.70
PSS density (%)	–	14.5	–	–	–	–	–	19.0	–	–	–	–	21.1	–
Volume change (%)	−22.9	−31.0	−46.4	−42.5	−41.2	−40.8	−42.4	−39.1	−47.3	−39.0	−48.3	−36.6	−37.9	−42.8
Major elements (wt%)														
SiO_2	72.66	70.10	64.92	64.57	68.65	67.53	66.52	67.86	64.63	66.25	65.08	68.99	68.16	66.18
TiO_2	0.47	0.52	0.66	0.62	0.61	0.61	0.63	0.59	0.68	0.59	0.70	0.57	0.58	0.63
$A1_2O_3$	12.99	13.74	16.49	16.32	14.11	14.74	15.63	14.99	17.51	16.57	16.76	15.38	14.69	16.27
Fe_2O_3	3.98	5.16	5.78	6.42	5.34	5.57	5.58	5.34	4.96	4.73	4.99	4.50	5.34	5.30
MnO	0.07	0.09	0.26	0.29	0.19	0.22	0.21	0.07	0.04	0.04	0.05	0.04	0.14	0.07
MgO	1.06	1.77	2.36	2.34	2.02	2.28	2.41	1.54	1.49	1.38	1.56	1.27	2.02	1.58
CaO	0.36	0.39	0.39	0.26	0.47	0.53	0.35	0.63	0.45	0.90	0.79	0.43	0.43	0.40
Na_2O	3.22	1.79	2.05	1.98	2.22	1.75	2.09	2.57	2.46	2.59	2.89	2.53	2.03	2.67
K_2O	2.37	2.93	3.29	3.49	3.04	2.93	2.92	2.79	3.74	3.39	3.14	3.04	2.91	3.33
P_2O_5	0.08	0.07	0.12	0.08	0.10	0.08	0.09	0.08	0.10	0.10	0.12	0.09	0.09	0.10
LOI	2.74	3.45	3.70	3.63	3.27	3.77	3.57	3.54	3.94	3.46	3.93	3.16	3.61	3.47
Trace elements (ppm)														
Ba	419	268	150	219	216	196	130	314	345	381	276	330	188	257
Ni	35.4	41.3	46.9	43.6	38.0	40.5	36.9	35.5	22.6	23.3	33.1	28.3	38.3	31.8
Cu	31.6	93.8	102.8	117.5	92.0	100.8	104.5	56.9	34.6	16.4	39.7	39.5	69.1	45.1
Zn	81	109	117	126	110	111	120	119	105	99	127	111	115	119
Pb	20.4	22.4	16.6	19.4	20.1	21.7	19.0	21.8	22.9	25.5	23.3	27.5	20.8	25.9
Th	12.9	12.9	15.1	15.5	12.4	16.6	15.4	13.5	16.9	15.4	14.5	14.9	12.5	15.5
Rb	96.6	132.9	136.0	149.4	123.0	122.9	124.2	117.5	161.4	138.9	129.7	127.6	126.6	137.8
Sr	106	71	83	71	92	72	81	101	106	143	106	100	70	101
Y	21.5	18.4	23.5	22.1	20.0	22.0	21.7	19.9	25.4	24.1	24.4	23.7	23.3	27.0
Zr	256	140	184	170	159	178	174	197	223	264	206	220	225	217
Nb	9.2	8.4	10.3	10.3	9.2	10.4	10.0	9.4	12.5	10.7	10.2	9.8	8.6	11.1

(*continued on next page*)

A. Appendix (*continued*)

Type	Type II melange				Type I melange									
Sample No.	MH02	MU01	MU03	MU02	SB23	SB11a	SB09a	SB09b	SB08a	SB07a	SB07b	SB07c	SB06a	SB06b
Grain density (g/cm^3)	2.70	2.70	2.70	2.70	2.68	2.69	2.67	2.70	2.68	2.72	2.65	2.70	2.71	2.70
PSS density (%)	–	20.5	–	–	25.93	8.80	–	3.27	0.43	0.68	–	–	–	6.05
Volume change (%)	−48.2	−31.1	−49.7	−16.9	−9.8	−11.7	6.8	28.4	6.2	−18.2	15.6	−17.7	−10.5	20.8
Major elements (wt%)														
SiO_2	63.66	69.59	64.34	72.03	65.31	67.91	72.99	69.91	71.39	66.68	74.18	66.35	67.63	71.88
TiO_2	0.69	0.52	0.71	0.43	0.63	0.64	0.53	0.44	0.53	0.68	0.49	0.68	0.62	0.46
$A1_2O_3$	17.25	12.78	16.18	11.59	17.15	14.89	12.98	12.68	13.18	15.91	12.88	16.15	14.64	11.28
Fe_2O_3	5.63	5.19	6.21	4.45	4.89	4.73	3.85	4.67	3.37	5.81	3.40	5.40	4.96	4.79
MnO	0.08	0.33	0.33	0.36	0.04	0.03	0.03	0.03	0.04	0.07	0.03	0.06	0.08	0.06
MgO	1.80	1.88	2.55	1.70	1.44	1.62	1.36	1.36	1.17	2.04	1.32	2.13	1.67	1.46
CaO	0.37	0.32	0.35	0.41	0.24	0.70	0.37	0.57	0.74	0.38	0.36	0.51	0.83	1.09
Na_2O	2.65	2.29	1.59	1.86	3.05	1.85	1.85	2.22	2.48	1.75	1.83	1.60	1.74	1.82
K_2O	3.65	2.24	3.49	2.24	3.53	3.14	2.46	2.16	2.67	3.06	2.41	3.18	3.19	1.94
P_2O_5	0.11	0.08	0.12	0.06	0.11	0.08	0.09	0.08	0.07	0.10	0.08	0.09	0.10	0.07
LOI	4.11	4.79	4.13	4.87	3.62	4.42	3.50	5.88	4.35	3.52	3.04	3.86	4.54	5.15
Trace elements (ppm)														
Ba	250	204	146	322	273	462	290	341	295	376	342	384	431	347
Ni	34.1	43.5	49.2	33.0	24.3	29.2	20.3	22.5	16.2	37.3	19.5	34.3	35.3	30
Cu	45.5	71.4	104.0	69.1	31.7	33	18.8	12	17.6	61.7	20	68.8	35.9	21.2
Zn	129	104	141	99	94	108	89	69	81	111	96	115	105	78
Pb	29.0	21.1	24.8	17.5	27.5	20.6	16.1	18.3	14.6	23.1	16.4	24	21.4	23.2
Th	16.0	9.2	16.5	9.1	16	13.2	11.1	11.2	12.2	13.5	10.7	15.1	13.3	8.7
Rb	149	101	142	107	146	135	108	94	106	135	107	139	125	85
Sr	72.9	71.7	53.4	65.1	89	119.2	98.9	123.4	100.8	57.1	69.3	67.6	97.7	115.3
Y	26.1	18.1	23.9	15.5	26.7	23.4	18.8	18.7	18	23.8	18	20.8	23.4	15.9
Zr	221	177	203	166	279	220	214	282	196	190	235	192	202	200
Nb	11.3	6.8	11.1	6.4	11.5	10.3	8.3	7.6	8.7	11.1	7.7	11.2	10	6.6

References

Archard, J., 1953. Contact and rubbing of flat surface. Journal of Applied Physics 24, 981–988.

Bjorlykke, K., Ramm, M., Saigal, G.C., 1989. Sandstone diagenesis and porosity modification during basin evolution. Geologische Rundschau 78 (1), 243–268.

Bolhar, R., Ring, U., 2001. Deformation history of the Yolla Bolly terrane at Leech Lake Mountain, Eastern belt, Franciscan subduction complex, California Coast Ranges. Geological Society of America Bulletin 113 (2), 181–195.

Brace, C.H., Paulding, B.W., Scholz, C., 1966. Dilatancy in the fracture of crystalline rocks. Journal of Geophysical Research 71, 3939–3953.

Bray, C.J., Karig, D.E., 1985. Porosity of sediments in accretionary prisms and some implications for dewatering processes. Journal of Geophysical Research 90 (NB1), 768–778.

Byrne, T., Fisher, D., 1987. Episodic growth of the Kodiak Convergent Margin. Nature 325 (6102), 338–341.

Coble, R.L., 1963. A model for boundary diffusion controlled creep in polycrystalline materials. Journal of Applied Physics 34, 1679–1682.

Condie, K.C., Dengate, J., Cullers, R.L., 1995. Behavior of rare-earth elements in a paleoweathering profile on granodiorite in the front range, Colorado, USA. Geochimica et Cosmochimica Acta 59 (2), 279–294.

Cowan, D.S., 1985. Structural styles in mesozoic and cenozoic melanges in the Western Cordillera of North-America. Geological Society of America Bulletin 96 (4), 451–462.

Ditullio, L., Byrne, T., 1990. Deformation paths in the shallow levels of an accretionary prism – the eocene Shimanto Belt of Southwest Japan. Geological Society of America Bulletin 102 (10), 1420–1438.

Evans, J.P., Chester, F.M., 1995. Fluid-rock interaction in faults of the San Andreas system: inferences from San-Gabriel fault rock geochemistry and microstructures. Journal of Geophysical Research 100 (B7), 13007–13020.

Goddard, J.V., Evans, J.P., 1995. Chemical changes and fluid-rock interaction in faults of crystalline thrust sheets, Northwestern Wyoming, USA. Journal of Structural Geology 17 (4), 533–547.

Goldschmidt, V., 1954. Oxford University Press, Geochemistry.

Grant, J.A., 1986. The isocon diagram – a simple solution to Gresens equation for Metasomatic alteration. Economic Geology 81 (8), 1976–1982.

Gratier, J.P., Jenatton, L., 1984. Deformation by solution-deposition, and re-equilibration of fluid inclusions in crystals depending on temperature, internal pressure and stress. Journal of Structural Geology 6, 189–200.

Gresens, R., 1967. Composition-volume relationships of metasomatism. Chemical Geology 2, 47–65.

Hibberd, J., Karig, D., Taira, A., 1992. Anomalous structural evolution of the Shimanto Accretionary Prism at Murotomisaki, Shikoku Island, Japan. Island Arc 1, 133–147.

Ikesawa, E., Kimura, G., Sato, K., Ikehara-Ohmori, K., Kitamura, Y., Yamaguchi, A., Ujiie, K., Hashimoto, Y., 2005. Tectonic incorporation of the upper part of oceanic crust to overriding plate of a convergent margin: an example from the Cretaceous – early Tertiary Mugi Mélange, the Shimanto Belt, Japan. Tectonophysics 401 (3–4), 217–230.

Ishida, K., 1998. Lithostratigraphy and radiolation age of the Shimanto Supergroup, East Sikoku. Journal of Osaka microfossil research group, Special Issue 11, 189–209.

Kitamura, Y., Sato, K., Ikesawa, E., Ikehara-Ohmori, K., Kimura, G., Kondo, H., Ujiie, K., Onishi, C.T., Kawabata, K., Hashimoto, Y., Mukoyoshi, H., Masago, H., 2005. Melange and its seismogenic roof decollement: a plate boundary fault rock in the subduction zone – an example from the Shimanto Belt, Japan. Tectonics 24, TC5012, doi:10.1029/2004TC001635.

Maghraoui, M.E., Joron, J.L., Raimbault, L., Treuil, M., 2002. Element mobility during metasomatism of granitic rocks in the Saint-Chély d'Apcher area (Lozere, France). Environment International 28 (5), 349–357.

Matsuda, T., Omura, K., Ikeda, R., Arai, T., Kobayashi, K., Shimada, K., Tanaka, H., Tomita, T., Hirano, S., 2004. Fracture-zone conditions on a recently active fault: insights from mineralogical and geochemical analyses of the Hirabayashi NIED drill core on the Nojima fault, southwest Japan, which ruptured in the 1995 Kobe earthquake. Tectonophysics 378 (3–4), 143–163.

Matsumura, M., Hashimoto, Y., Kimura, G., Ohmori-Ikehara, K., Enjohji, M., Ikesawa, E., 2003. Depth of oceanic-crust underplating in a subduction

zone: inferences from fluid-inclusion analyses of crack-seal veins. Geology 31 (11), 1005–1008.

Minshull, T., White, R., 1989. Sediment compaction and fluid migration in the Makran accretionary prism. Journal of Geophysical Research 94 (B6), 7387–7402.

Moore, J.C., 1992. Fluids in accretionary prisms (Reviews of Geophysics, vol. 30, p. 113, 1992). Reviews of Geophysics 30 (4), 353–353.

Morgan, J.K., Karig, D.E., 1995. Kinematics and a balanced and restored cross-section across the toe of the Eastern Nankai accretionary prism. Journal of Structural Geology 17 (1), 31–45.

Mori, K., Taguchi, K., 1988. Examination of the low-grade metamorphism in the Shimanto belt by vitrinite reflectance. Modern Geology 12, 325–339.

Niemeijer, A.R., Spiers, C.J., Bos, B., 2002. Compaction creep of quartz sand at 400–600 °C: experimental evidence for dissolution-controlled pressure solution. Earth and Planetary Science Letters 195, 261–275.

O'Hara, K., 1988. Fluid flow and volume loss during mylonitization: an origin for phyllonite in an overthrust setting, North Carolina, U.S.A. Tectonophysics 156, 21–36.

Ohmori, K., Taira, A., Tokuyama, H., Sakaguchi, A., Okamura, M., Aihara, A., 1997. Paleothermal structure of the Shimanto accretionary prism, Shikoku Japan: role of an out-of-sequence thrust. Geology 25 (4), 327–330.

Olsen, S.N., Grant, J.A., 1991. Isocon analysis of migmatization in the front range, Colorado, USA. Journal of Metamorphic Geology 9 (2), 151–164.

Osozawa, S., 2005. The Miocene Nabae complex in not a tectonic melange. The 112nd Annual Meeting of the Geological Society of Japan. Geological Society of Japan, University of Kyoto, Japan. 126.

Petersson, J., Eliasson, T., 1997. Mineral evolution and element mobility during episyenitization (dequartzification) and albitization in the postkinematic Bohus granite, southwest Sweden. Lithos 42 (1–2), 123–146.

Raj, R., 1982. Creep in polycrystalline aggregates by matter transport through a liquid-phase. Journal of Geophysical Research 87, 4731–4739.

Ring, U., Brandon, M.T., 1999. Ductile Deformation and Mass Loss in the Franciscan Subduction Complex: Implications for Exhumation Processes in Accretionary Wedge. Exhumation Processes: Normal Faulting, Ductile Flow and Erosion. Geological Society, London, Special Publications.

Rutter, E.H., 1976. Kinetics of rock deformation by pressure solution. Mathematical Physical and Engineering Sciences 283, 203–219.

Rutter, E.H., 1983. Pressure solution in nature, theory and experiment. Journal of the Geological Society 140 (SEP), 725–740.

Sakaguchi, A., 1996. High paleogeothermal gradient with ridge subduction beneath the Cretaceous Shimanto accretionary prism, southwest Japan. Geology 24 (9), 795–798.

Sakaguchi, A., 1999. Thermal structure and paleo-heat flow in the Shimanto accretionary prism, Southwest Japan. Island Arc 8 (3), 359–372.

Sakai, H., 1987. Storm Barnacle beds and their deformation in the Muroto-Misaki olistostrome and melange complex, Shikoku. Journal of the Geological Society of Japan 93 (8), 617–620.

Scholz, C.H., Dawers, N.H., Yu, J.Z., Anders, M.H., 1993. Fault growth and fault scaling laws-preliminary results. Journal of Geophysical Research 98, 21951–21961.

Schutjens, P.M.T.M., 1991. Experimental compaction of quartz sand at low effective stress and temperature consition. Journal of the Geological Society, London 148, 527–539.

Spiers, C.J., Schutjens, P.M.T.M., Brzesowsky, R.H., Peach, C.J., Liezenberg, J.L., Zwart, H.J., 1990. Experimental Determination of Constitutive Parameters Governing Creep of Rocksalt by Pressure Solution. Geological Society, Special Publication.

Streit, J.E., Cox, S.F., 1998. Fluid infiltration and volume change during mid-crustal mylonitization of Proterozoic granite, King Island, Tasmania. Journal of Metamorphic Geology 16 (2), 197–212.

Tada, R., Siever, R., 1989. Pressure solution during diagenesis. Annual Review of Earth and Planetary Sciences 17, 89–118.

Taira, A., Tashiro, M., Okamura, M., Katto, J., 1980. The Geology of the Shimanto Belt in Kochi Prefecture, Shikoku, Japan. Memorial Issue for Prof. J. Katto., pp. 319–389.

Taira, A., Katto, J., Tashiro, M., Okamura, M., Kodama, K., 1988. The Shimanto belt in Shikoku, Japan – evolution of Cretaceous to Miocene accretionary prism. Modern Geology 12, 5–46.

Tanaka, H., Fujimoto, K., Ohtani, T., Ito, H., 2001. Structural and chemical characterization of shear zones in the freshly activated Nojima fault, Awaji Island, southwest Japan. Journal of Geophysical Research 106, 8789–8810.

Tanaka, H., Omura, K., Matsuda, T., Ikeda, R., Kobayashi, K., Murakami, M., Shimada, K. in press. Architectural evolution of Nojima fault and identification of the active slip layer by Kobe earthquake. Journal of Geophysical Research, in press.

Ujiie, K., 1997. Off-scraping accretionary process under the subduction of young oceanic crust: the Shimanto belt of Okinawa island, Ryukyu arc. Tectonics 16 (2), 305–322.

Underwood, M., Laughland, M.M., Byren, T., Hibbard, J.P., DiTullio, L., 1992. Thermal evolution of the Tertiary Shimanto Belt, Muroto Peninsula, Shikoku, Japan. Island Arc 1, 116–132.

Underwood, M.B., Laughland, M.M., Kang, S.M., 1993. A comparison among organic and inorganic indicators of diagenesis and low-temperature metamorphism, Tertiary Shimanto Belt, Shikoku, Japan. Geological Society of America Special paper 273, 45–61.

Wang, W.B., Scholz, C.H., 1994. Wear processes during frictional sliding of rock – a theoretical and experimental-study. Journal of Geophysical Research 99 (B4), 6789–6799.

Widmer, T., Thompson, A.B., 2001. Local origin of high pressure vein material in eclogite facies rocks of the Zermatt-Saas Zone, Switzerland. American Journal of Science 301 (7), 627–656.

Wong, T.F., David, C., Zhu, W.L., 1997. The transition from brittle faulting to cataclastic flow in porous sandstones: mechanical deformation. Journal of Geophysical Research 102 (B2), 3009–3025.